Supplementary Information (SI) for Journal of Materials Chemistry A

Single Zn Atoms Anchored in Mesoporous N-Doped Carbon Rods Derived from Metal-Organic Frameworks for Enhanced Electrocatalytic Oxygen Reduction Reaction

Mengxue Ma[†a], *Zhuoya Pei*[†a], *Yuxin Peng*[a], *Rong Hua*[a], *Yuxing Ma*[a], *Weilong Wang*[b], *Xiaoxiang Xu*[b]*, *Xuepeng Zhang*[a], *Haoquan Zheng*[a, c]*

[a]Key Laboratory of Applied Surface and Colloid Chemistry, Ministry of Education, School of Chemistry and Chemical Engineering, Shaanxi Normal University, Xi'an 710119, China.

[b]Department of Otorhinolaryngology-Head and Neck Surgery, Zhongnan Hospital of Wuhan University, Wuhan, 430071, China.

[c]Shanghai Key Laboratory of High-resolution Electron Microscopy, ShanghaiTech University, Shanghai 201210, China

Correspondence Email: zhenghaoquan@snnu.edu.cn; zn003504@whu.edu.cn

[†]These authors contributed equally to this work.

1. Materials characterization

Scanning electron microscopy (SEM) images were recorded on a Hitachi SU8020 microscope. Transmission electron microscopy (TEM) measurements were performed by a JEOL JEM-7900F, the acceleration voltage is 200 kV. And energy dispersive X-ray spectroscopy (EDS) was used to observe the microstructure and the uniform dispersion of C, N, O, Zn in the catalyst. Aberration correction high-angle dark-filed scanning transmission electron microscope (AC HAADF-STEM) images were conducted on a Themis G2 300 microscope operated at 300 kV. Powder X-ray diffraction (PXRD) patterns were used to Bruker D8 Advance. Raman spectroscopy was performed on a HORIBA LabRAM Odyssey Raman spectrometer system (532 nm laser). X-ray photoelectron spectroscopy (XPS) spectra were recorded on Kratos Analytical Ltd AXIS ULTRA. N_2 adsorption-desorption isotherm and Brunauer-Emmett-Teller (BET) surface area with a Micromeritics/ASAP 2460 instrument to detect. Zn K-edge X-ray absorption spectra (XAS) were collected by easyXAFS300 + (easyXAFs company).

2. Electrochemical measurements for ORR

All electrochemical performance evaluations were carried out on the CHI 760E electrochemical workstation, utilizing a setup with three-electrode in a 0.1 M KOH solution. The carbon rod served as the counter electrode, while the Ag/AgCl electrode was used as the reference electrode. The working electrode was either a rotating disk electrode (RDE) (5 mm, 0.196 cm^2) or a rotating ring-disk electrode (RRDE) (5.61 mm, 0.247 cm^2), both coated with catalyst slurry. Among the ink of catalyst included 2 mg of the sample, 333 μL of water, 166 μL of ethanol, and 10 μL of 5 % Nafion solution, and was ultrasonicated for 30 min to obtain a homogeneous solution. The above ink was transferred 20 μL by using a pipette in twice, dropped onto the electrode surface, and dried naturally at room temperature, the total load of catalyst was 0.4 mg cm^{-2}. Before testing, introducing Ar or O_2 into the 0.1 M KOH solution for 30 min to eliminate dissolved oxygen in the electrolyte. Cyclic voltammetry (CV) measurements

were operated in Ar- or O_2-saturated with a scan rate of 50 mV s^{-1}. Linear sweep voltammetry (LSV) measurements were performed with a scan rate of 5 mV s^{-1} under different rotating speeds of 400 - 2025 rpm after 100 % IR compensation. The potentials of this experiment refer to reversible hydrogen electrode (RHE), $E_{RHE} = E_{Ag/AgCl} + 0.059$ pH + 0.197. The electron transfer number (n) was determined by RDE measurements by Koutecký-Levich (K-L) equation:

$$\frac{1}{j} = \frac{1}{j_l} + \frac{1}{j_k} = \frac{1}{B\omega^{1/2}} + \frac{1}{j_k}$$

$$B = 0.2nFC_0(D_0)^{2/3}v^{-1/6}$$

Where j, j_l, j_k represent the experimentally measured, diffusion limiting and kinetic current density, respectively. Ω is the rotation speed (rotations per minute, rpm), n is the electron transfer number, F is the Faraday constant (96485 C mol^{-1}), C_0 is the bulk concentration of O_2 in 0.1 M KOH (1.2×10^{-3} M), D_0 is the diffusion coefficient of O_2 in 0.1 M KOH (1.9×10^{-5} cm^2 s^{-1}), and v is the kinematic viscosity (0.01 cm^2 s^{-1}). The n and hydrogen peroxide yield (H_2O_2 %) also can calculated by RRDE measurements by the following equations:

$$n = \frac{4\,I_d}{I_d + \frac{I_r}{N}}$$

$$H_2O_2\,\% = \frac{200\,\frac{I_r}{N}}{I_d + \frac{I_r}{N}}$$

Where I_d and I_r are disk and ring current density, respectively. N is the collection efficiency of Pt ring (0.37).

The electrochemically active surface area (ECSA) was measured by CV at different scan rates of 20 – 100 mV s^{-1} in a non-Faradaic potential (1.07 – 1.17 V). The ECSA was calculated by following equation:

$$ECSA = C_{dl}/C_s$$

Where C_{dl} is double-layer capacitance by measured, C_s is the specific capacitance (0.03 mF cm^{-2}).

3. Zn-air battery measurements

All electrochemical performance tests of batteries were conducted on the CHI 660E electrochemical workstation. A polished round zinc plate serves as the anode of a Zn-air battery (thickness 0.25 mm, diameter 15 mm). And the gas diffusion layer (thickness 0.2 mm, 1.8 × 1.8 cm^2) and the loaded catalyst layer (thickness 0.2 mm, 1.5 × 1.5 cm^2) together form the cathode of the battery. The catalyst ink was prepared as follows: 2.5 mg of catalyst and 2.5 mg of RuO_2 were dispersed in 910 μL of ethanol, 50 μL of water, and 40 μL of Nafion (5 wt%), dissolved by ultrasound for 30 minutes, and 500 μL of the ink was dropped onto the surface of the loaded catalyst layer, with a catalyst loading of 2 mg cm^{-2}. The electrolyte was composed of a mixture of 6 M KOH and 0.2 M $Zn(NO_3)_2 \cdot 6H_2O$. The rate capacities were evaluated by galvanostatic discharge at various current density of 2, 5, 10, 20 and 50 mA cm^{-2} and back to 2 mA cm^{-2}. And the cycle time of each battery was 10 min during long-term charge-discharge cycle test.

4. Computational details

All density functional theory (DFT) periodic calculations were conducted using the Vienna Ab-initio Package (VASP).[1, 2] The functional proposed by Perdew, Burke, and Emzerhof (PBE) was utilized for these calculations. Interactions were modeled using the projector augmented wave (PAW) potential, while the Kohn-Sham one-electron valence states were expanded in a plane wave basis with a cutoff energy set at 500 eV.[3-5]

Regarding the balance between structural modeling accuracy and computation cost, we have constructed the model based on either pristine Zn-MCRs or NC surface. The vacuum thickness is set to the value greater than 15 Å to ensure sufficient separation between the two opposite surface effect. To optimize computational

efficiency, the Monkhorst-Pack reciprocal space integration was carried out using Gamma-centered k-points with a grid of 3 × 3 × 1. The Hellmann-Feynman forces were deemed converged when was set as smaller than 0.03 eV/Å. The electronic energy was considered self-consistent if the energy change was less than 10^{-5} eV and the convergence criterion for frequency calculation is that the energy is less than 10^{-6} eV.

In this study, the Gibbs free energy was also calculated. The zero-point energy (ZPE) correction was applied using methods previously reported in the literature. During the DFT process, we determined the Gibbs free energy using the following equations:

$$G^0 = E_{DFT} + ZPE - TS^0$$

Where G^0 is the Gibbs free energy, E_{DFT} is total free energy, ZPE is the vibration energy; TS^0 is the entropy change (T = 298.15 K). The ORR process proceeds via the following pathway:

$$O_2\ (g) + * \rightarrow OO^* \quad (1)$$

$$OO^* + H^+ + e^- \rightarrow OOH^* \quad (2)$$

$$OOH^* + H^+ + e^- \rightarrow O^* + H_2O\ (l) \quad (3)$$

$$O^* + H^+ + e^- \rightarrow HO^* + O_2\ (g) + H^+ + e^- \quad (4)$$

$$HO^* + H^+ + e^- \rightarrow H_2O^* \quad (5)$$

$$H_2O^* \rightarrow * + H_2O\ (l) \quad (6)$$

The Standard Hydrogen electrode (SHE) model was used to calculate the change of each elementary step (OO*, OOH*, O*, HO*, H_2O*, *) in Gibbs free energy. The chemical potential of proton-electron pair is equal to one half of H_2.[6]

Table S1. ICP-OES of the metal contents of the samples

Sample	Zn (wt %)
Zn-MCRs	6.6
Zn-CRs	7.2
MCRs	0.47
NC	5.0

The Zn content in both Zn-CRs and Zn-MCRs is higher than that in NC, demonstrating that the introduction of the PDA composite monomicelles layer effectively captures a portion of the Zn and successfully anchors it onto the surface of the ZIF-R.

Table S2. BET surface area of the samples

	Zn-MCRs (m^2 g^{-1})	**NC (m^2 g^{-1})**
S_{BET}	616.8	543.6
S_{micro}	470.0	462.2
S_{meso}	146.8	81.4

Zn-MCRs exhibit a higher specific surface area and possess more mesoporous sections (146.8 m^2 g^{-1}) compared to NC (81.4 m^2 g^{-1}), thereby proving the successful introduction of monomicelles.

Table S3. EXAFS fitting parameters at the Zn K-edge for various samples

samples	path	CN	R (Å)	σ^2 (Å^2)	ΔE_0 (eV)	R factor
Zn foil	Zn-Zn1	6	2.65	0.0118 ± 0.0020	1.50 ± 1.59	0.0032
	Zn-Zn2	6	2.80	0.0243 ± 0.0074		
ZnO	Zn-O	3.8 ± 0.9	1.96	0.0045 ± 0.0038	2.79 ± 3.04	0.0053
Zn-MCRs	Zn-N	3.9 ± 0.6	2.00	0.0153 ± 0.0023	-1.15 ± 1.45	0.0160

CN, coordination number; R, distance between absorber and backscatter atoms; σ^2, Debye-Waller factor to account for both thermal and structural disorders; ΔE_0, inner potential correction; R factor indicates the goodness of fit.

Table S4. Performance comparison of Zn-based electrocatalysts for ORR catalysts in alkaline

Catalyst	$E_{1/2}$ (vs RHE) (mV)	Reference
Zn-MCRs	**873**	**This work**
Zn-SAs/UNCNS	910	*Chem Catalysis* 2022, **2**, 836-852
S-Zn-N-C-950	890	*Adv. Funct. Mater.* 2024, **34**, 2311337
Zn-B/N-C	886	*Angew. Chem. Int. Ed.* 2021, **60**, 181-185
Zn-N_4-O	884	*Adv. Sci.* 2023, **10**, 2302152
ZnNC	880	*Angew. Chem. Int. Ed.* 2023, **62**, e202216041
ZnNC	880	*Angew. Chem.* 2023, **135**, e202216041
Zn-N-C	873	*Angew. Chew. Int. Ed.* 2019, **58**, 7035
Zn-NC/GD	860	*Carbon* 2022, **186**, 589-598
Zn-N-C	860	*Chin. Chem. Lett.* 2020**, 31** 1207-1212
ZnNC	857	*Nat. Commun.* 2019, **10**, 2623
Zn-N-C-2	850	*J. Colloid Interface Sci.* 2023, **650**, 934-942
Zn/NC-2	845	*Inorg. Chem.* 2023, **62**, 16547-16553
ZnNx/BP	593	*Adv. Funct. Mater.* 2017, **27**, 1700802

Table S5. The Gibbs free energy change of the reaction in step 4 (ΔG_4) of the NC material occurring at the α-C and β-C sites

(eV)	**ΔG_4**
NC-C_α	-1.26
NC-C_β	-1.21

Table S6. The Gibbs free energy change of the reaction in step 1 (ΔG_1) of the Zn-MCRs material occurring at the α-C and β-C sites

(eV)	**ΔG_1**
Zn-MCRs-C_α	0.84
Zn-MCRs-C_β	1.49

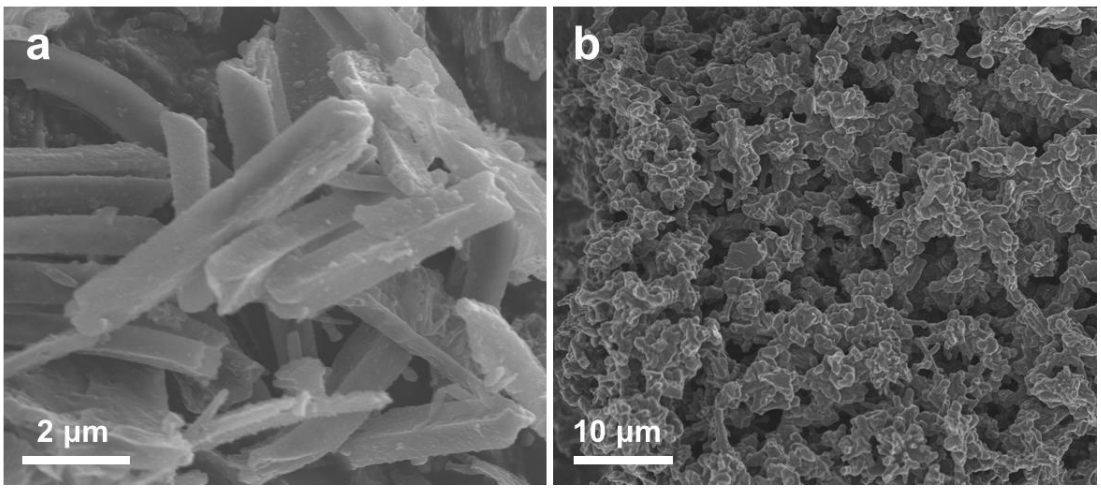

Fig. S1. SEM images of Zn-CR (a), and NC (b).

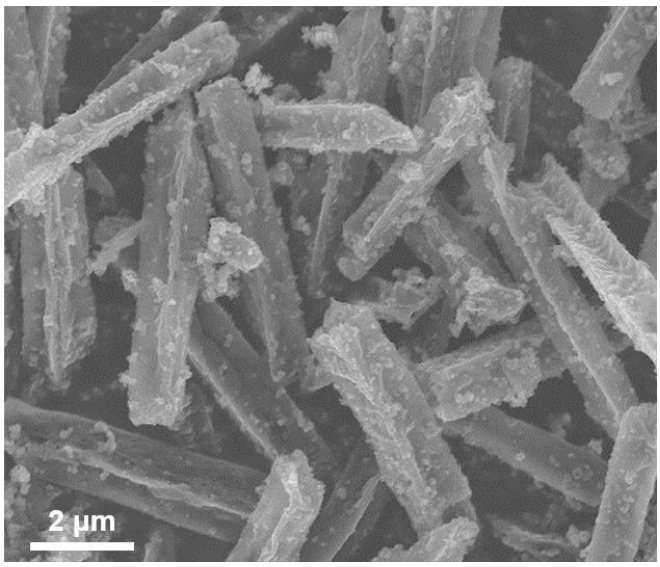

Fig. S2. SEM image of Zn-MCR.

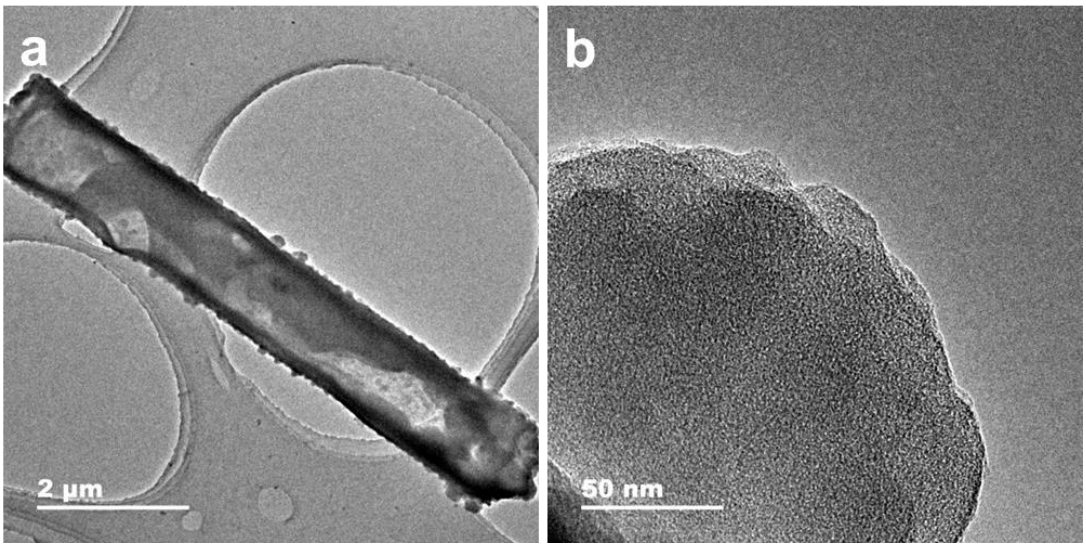

Fig. S3. TEM images of Zn-CR.

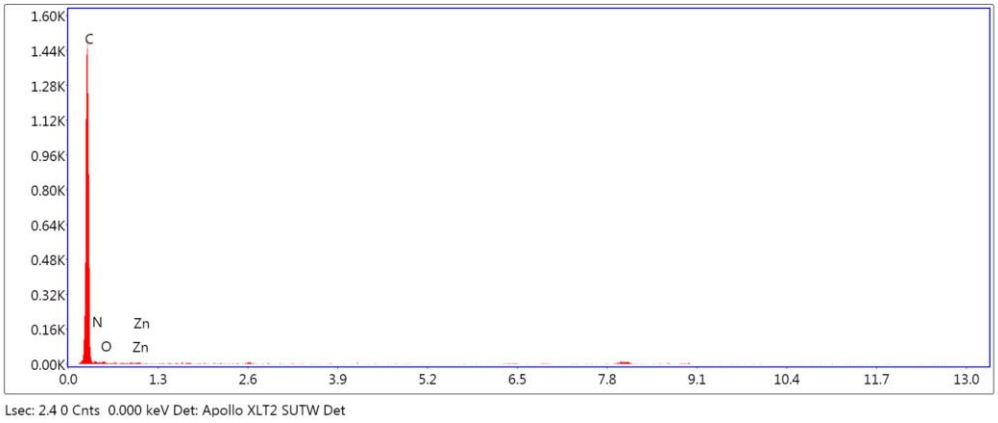

Fig. S4. EDS spectrum of MCR.

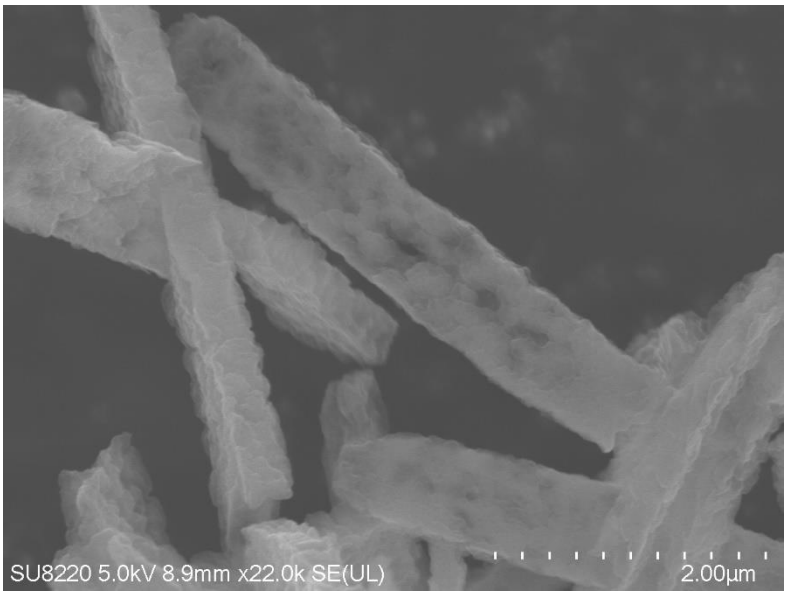

Fig. S5. SEM image of MCR.

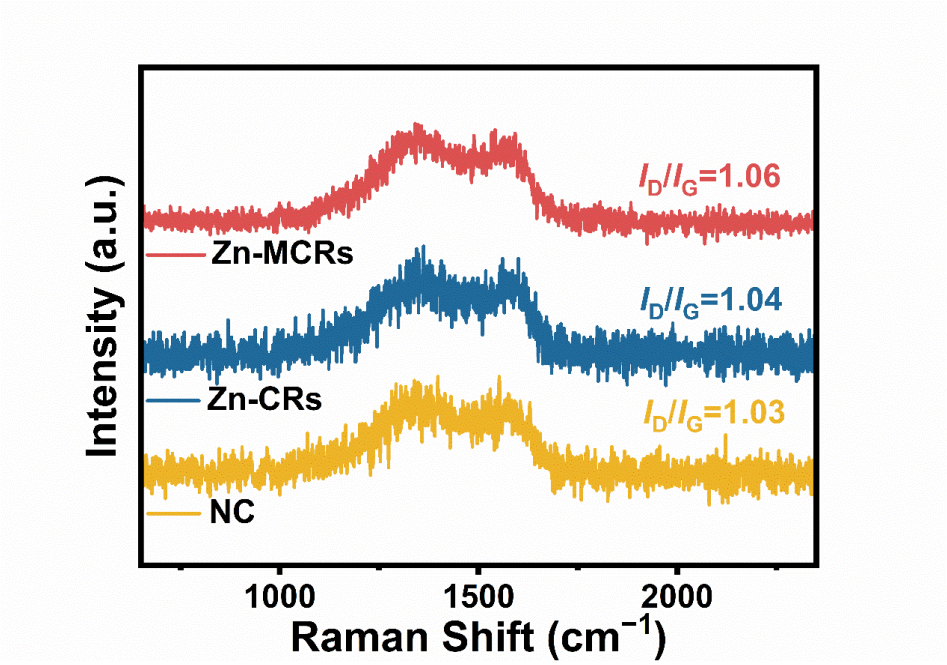

Fig. S6. Raman spectra of Zn-MCR, Zn-CR, and NC.

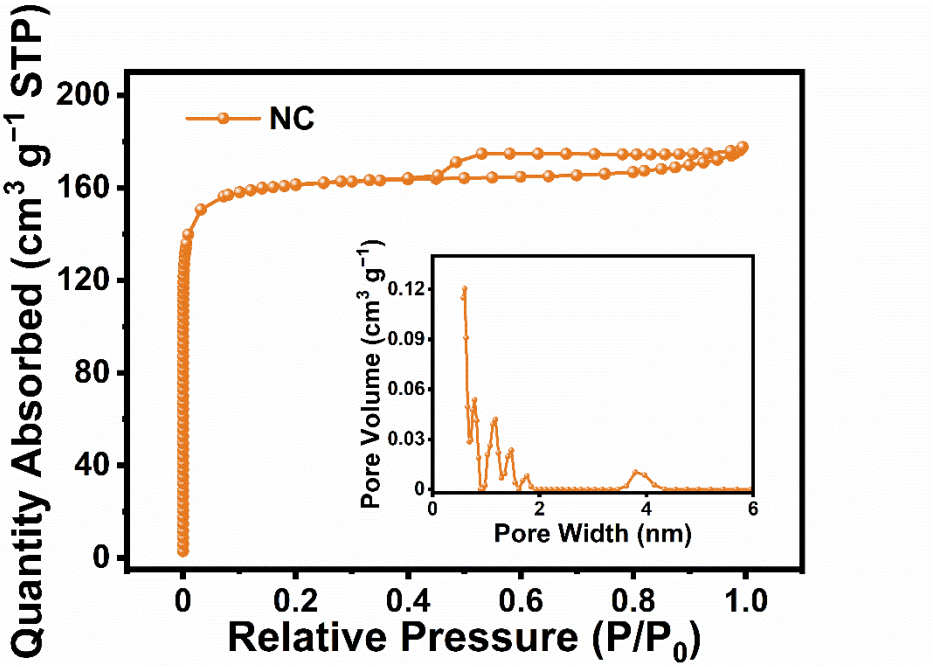

Fig. S7. N_2 adsorption-desorption isotherms, and corresponding pore size distribution curves of NC.

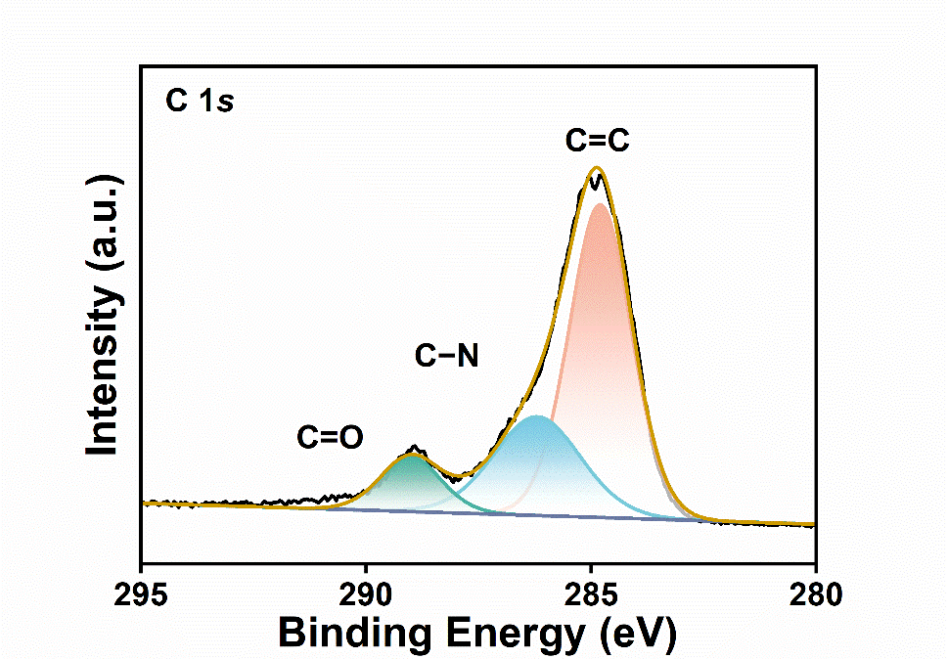

Fig. S8. High-resolution C1*s* XPS spectra of Zn-MCRs.

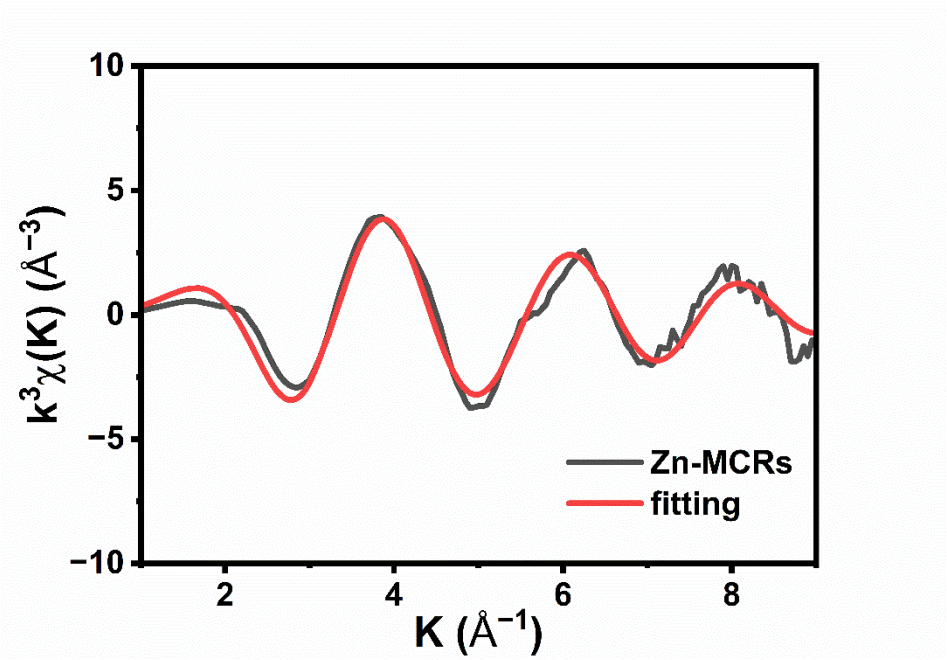

Fig. S9. Zn K-edge k^3 -weighted EXAFS fitting curves of Zn-MCRs at K-space.

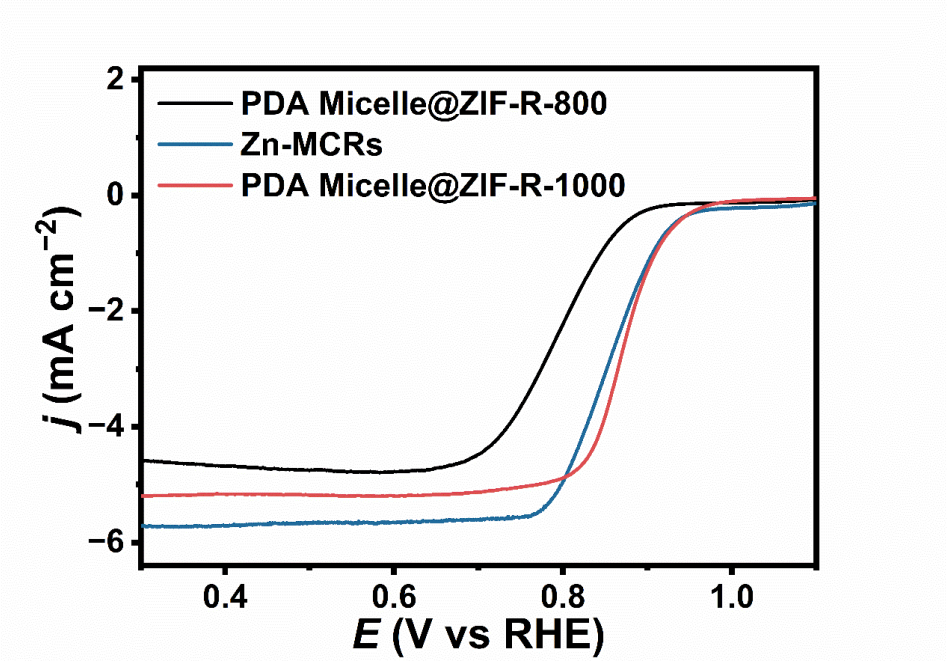

Fig. S10. LSV curves of Zn-MCRs at different pyrolysis temperatures of 800 °C, 900 °C, and 1000°C.

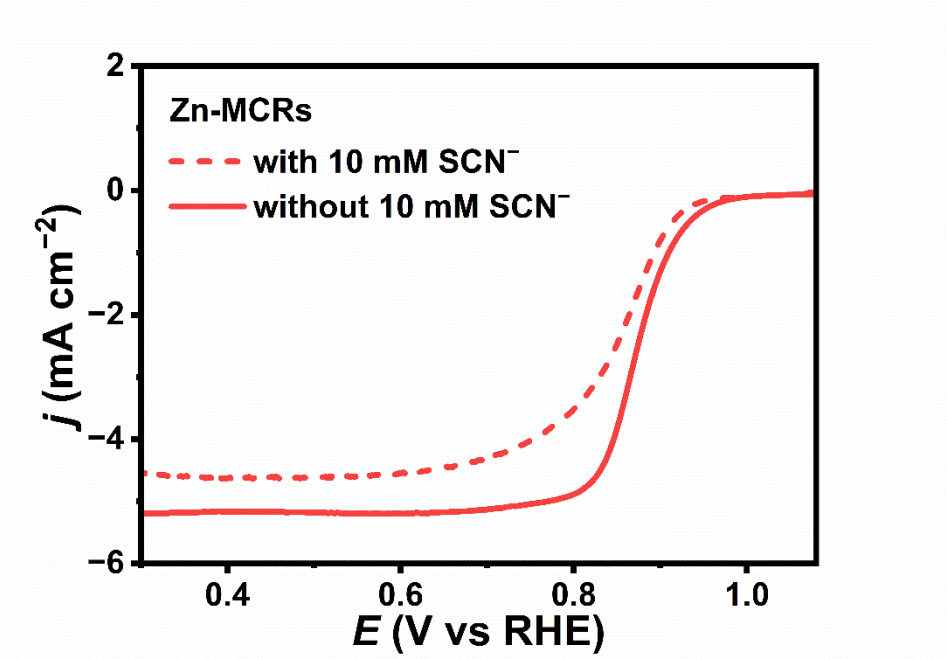

Fig. S11. LSV polarization curves of Zn-MCRs catalysts in O_2-saturated KOH before and after adding KSCN solution.

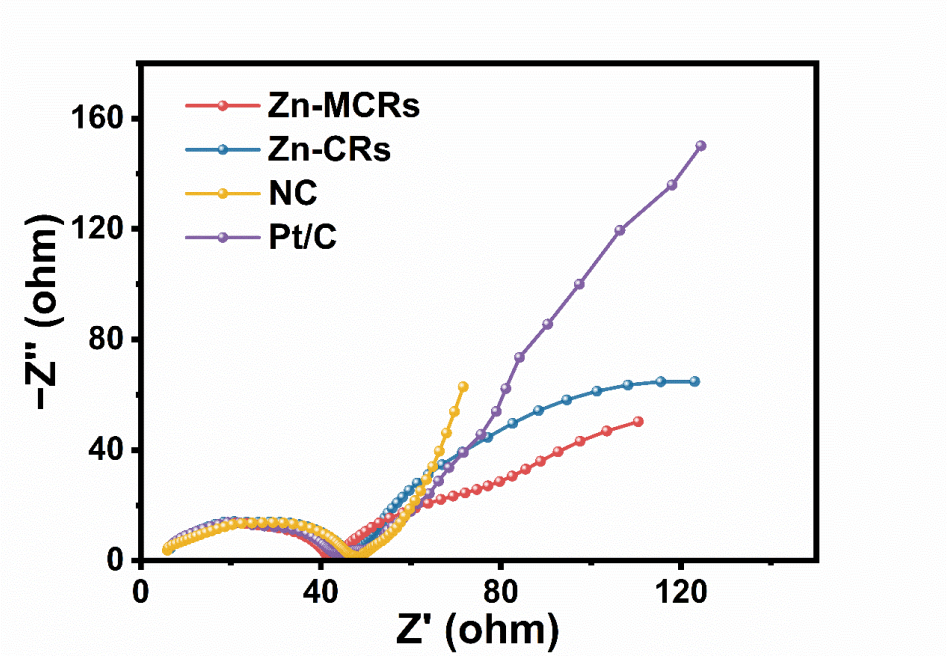

Fig. S12. EIS plots of Zn-MCRs in 0.1 M KOH.

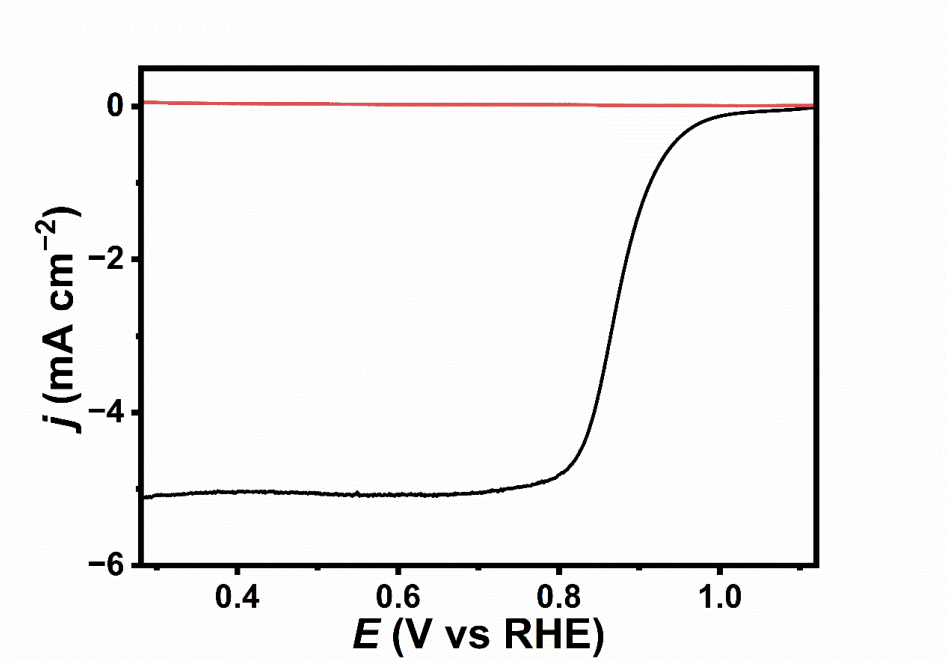

Fig. S13. LSV curves of Zn-MCRs by RRDE measurements.

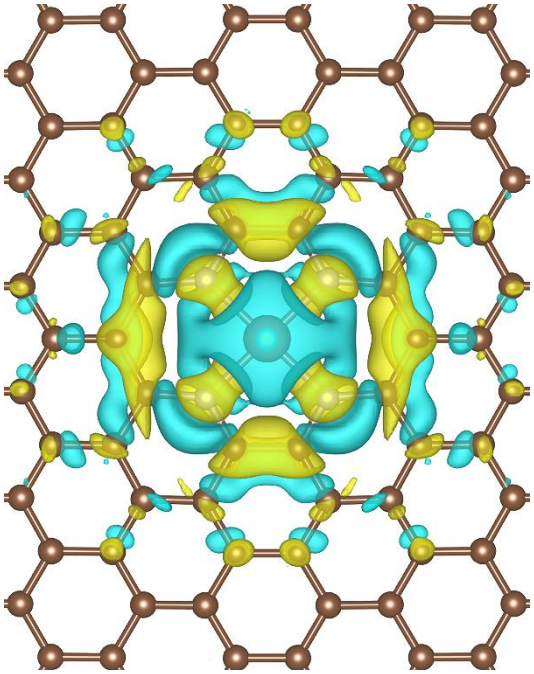

Fig. S14. The charge difference density diagram of Zn-MCRs. (isosurface level: 0.001 e $Bohr^{-3}$).

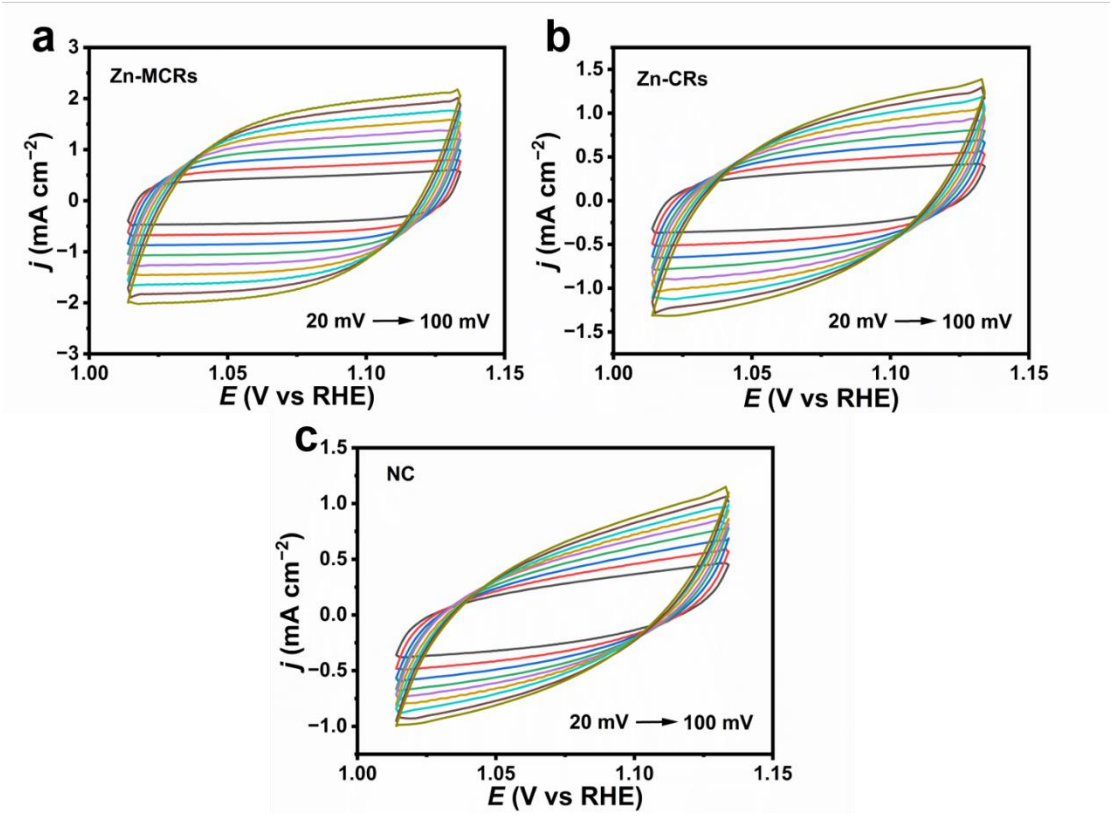

Fig. S15. CV curves at different scan rates of (a) Zn-MCRs, (b) Zn-CRs, and (c) NC in 0.1 M KOH.

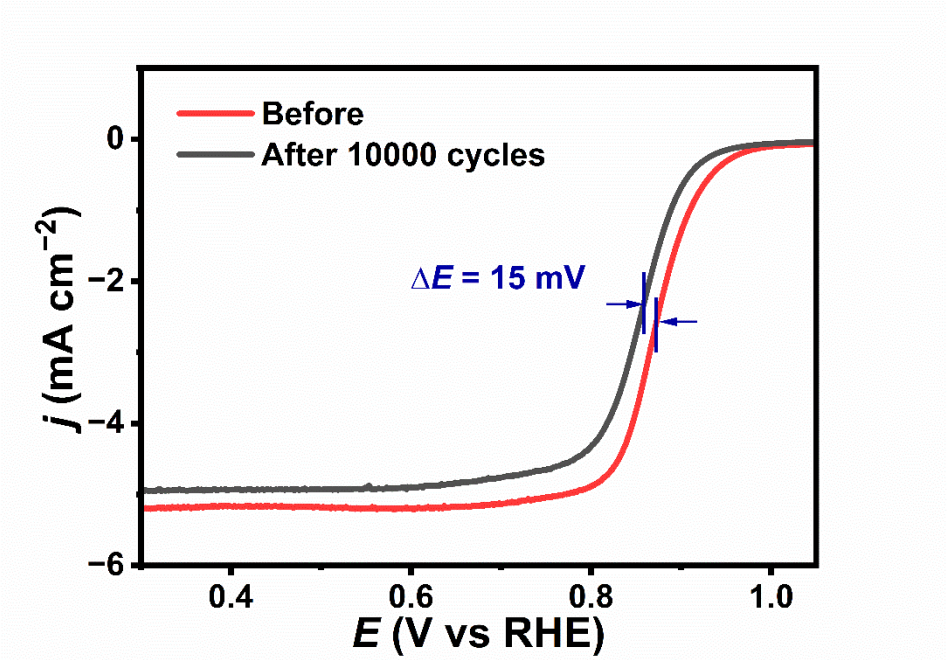

Fig. S16. ORR polarization curves before and after 10000 CV cycles of Zn-MCRs.

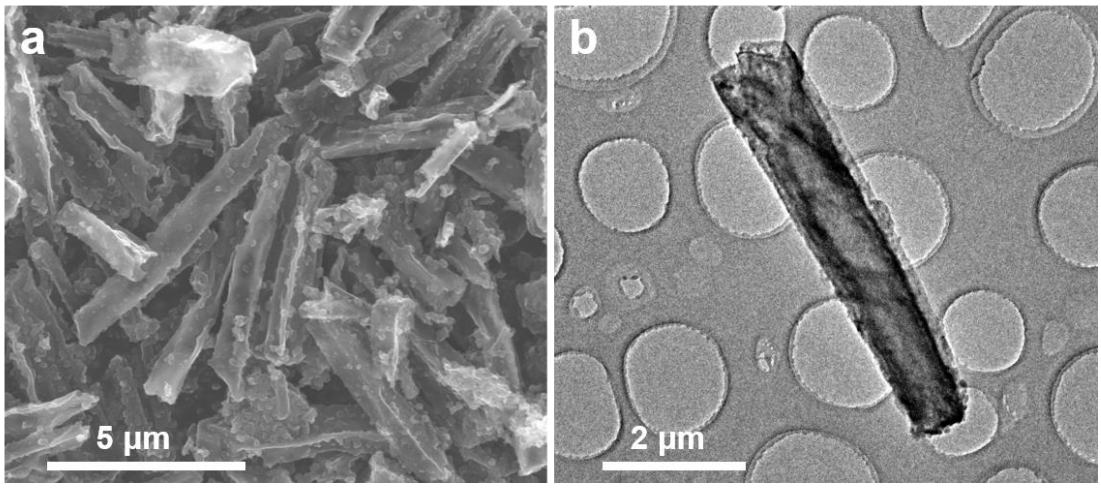

Fig. S17. SEM image (a) and TEM image (b) of Zn-MCRs after ORR.

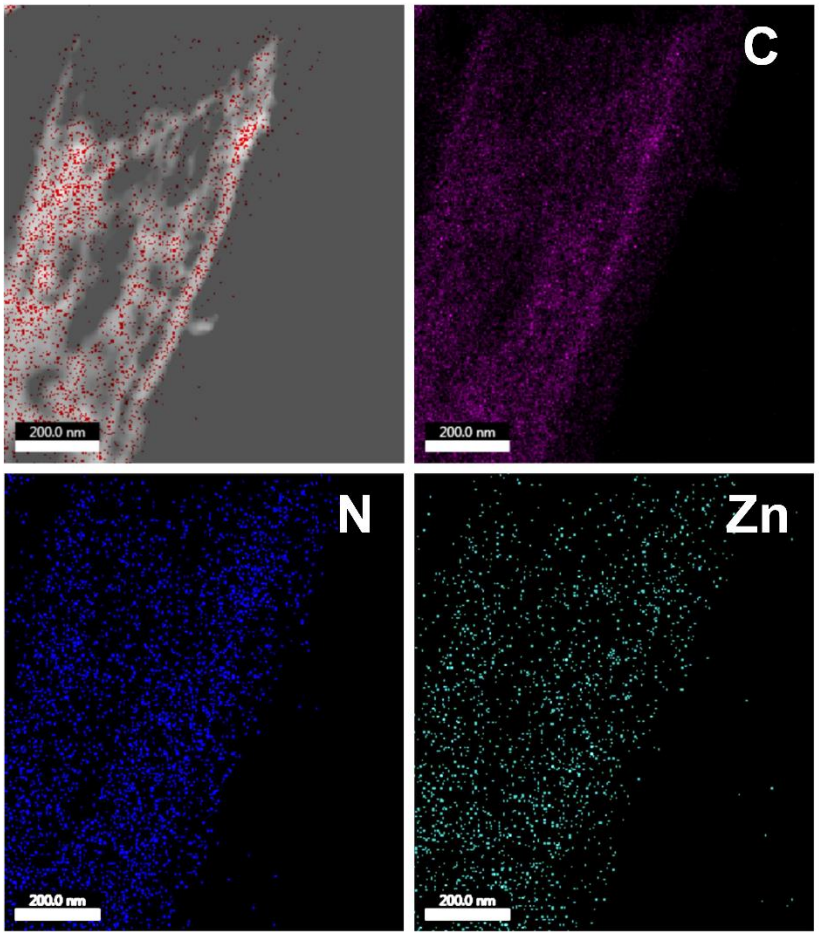

Fig. S18. EDS-mapping of Zn-MCRs after ORR.

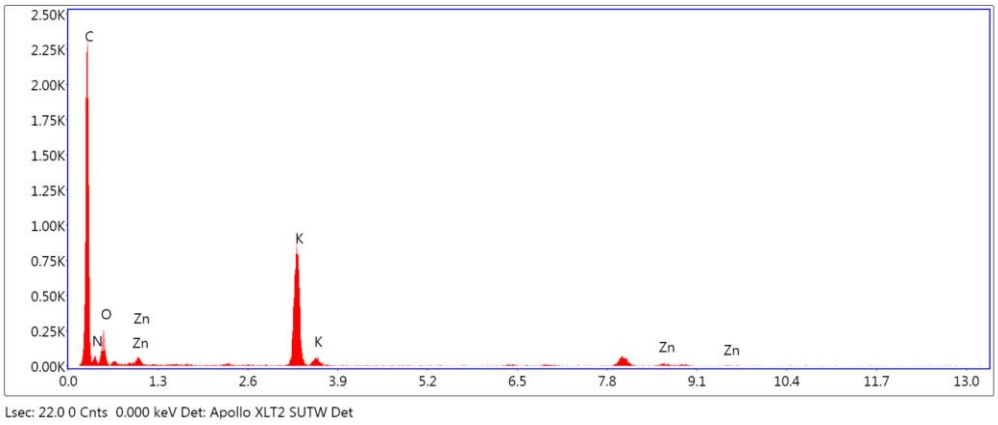

Fig. S19. EDS spectrum of Zn-MCRs after ORR.

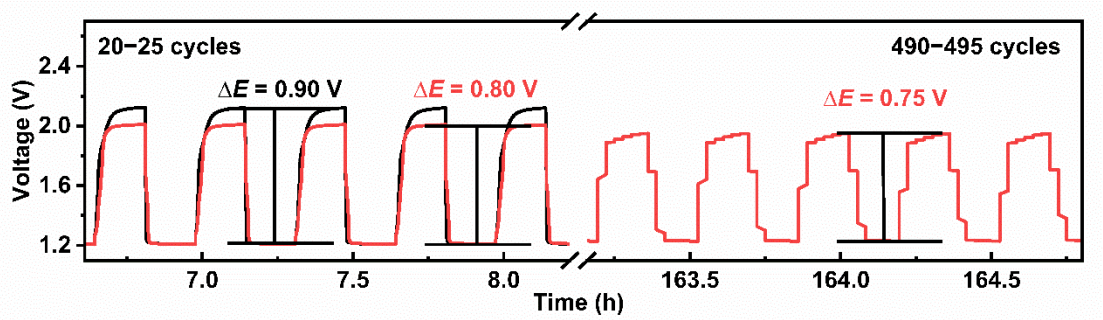

Fig. S20 Charge-discharge voltage difference at different times of ZABs assembled with Zn-MCRs + RuO_2 and Pt/C + RuO_2.

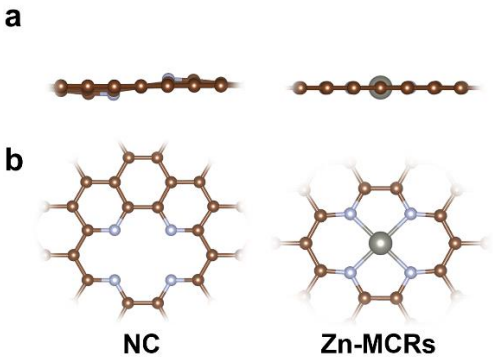

Fig. S21. (a) Side view and (b) top view of the optimized models of NC material and Zn-MCRs material.

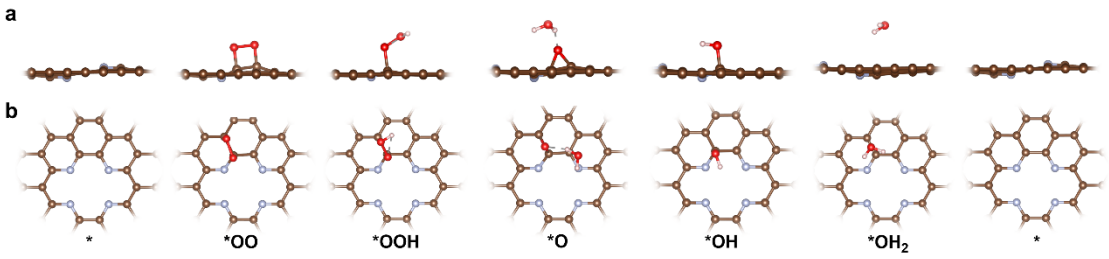

Fig. S22. (a) Side view and (b) top view of the optimized structures of each ORR intermediate at the C site on the NC material.

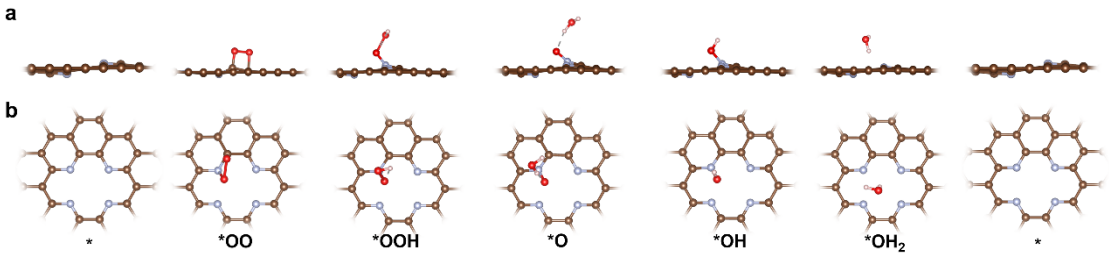

Fig. S23. (a) Side view and (b) top view of the optimized structures of each ORR intermediate at the N site on the NC material.

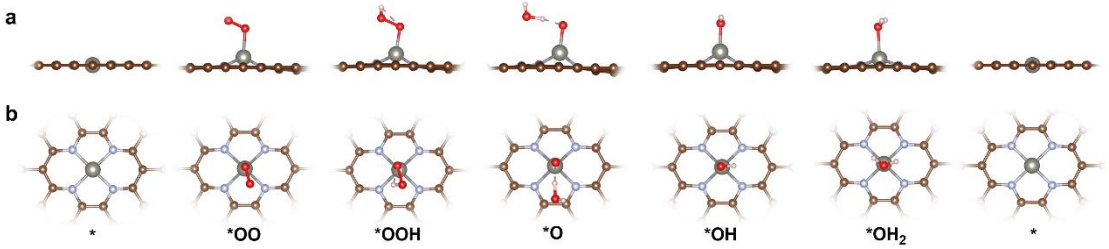

Fig. S24. (a) Side view and (b) top view of the optimized structures of each ORR intermediate at the Zn site on the Zn-MCRs material.

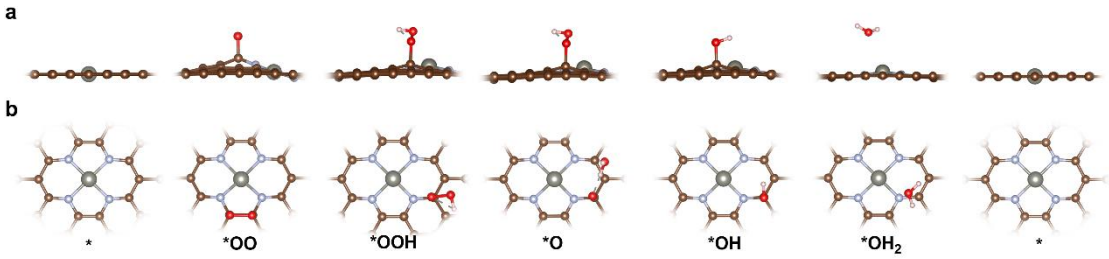

Fig. S25. (a) Side view and (b) top view of the optimized structures of each ORR intermediate at the C site on the Zn-MCRs material.

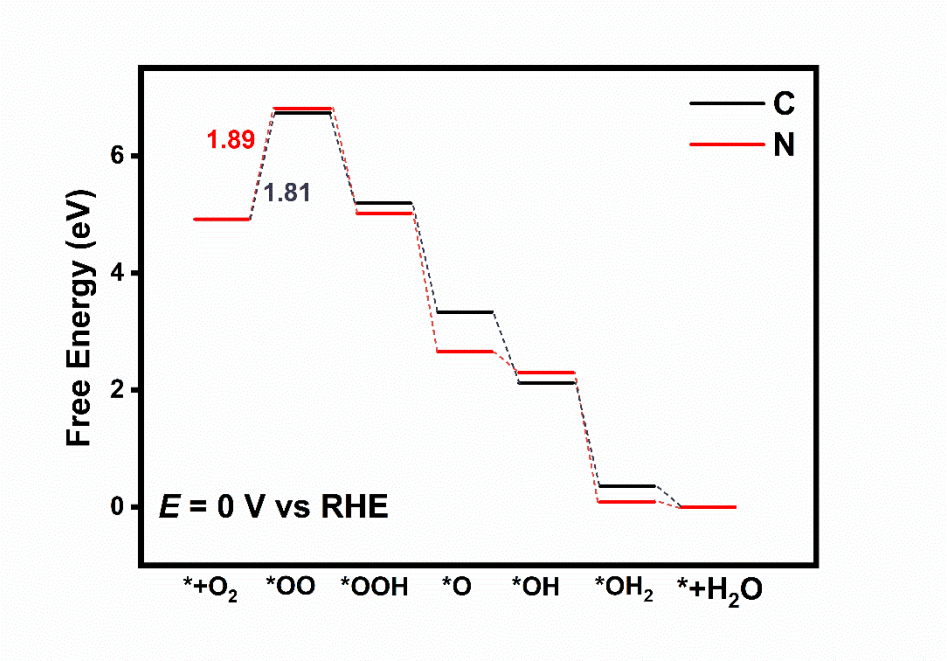

Fig. S26. The simulated energy barrier diagram at the N and C sites of the NC model at U = 0 V.

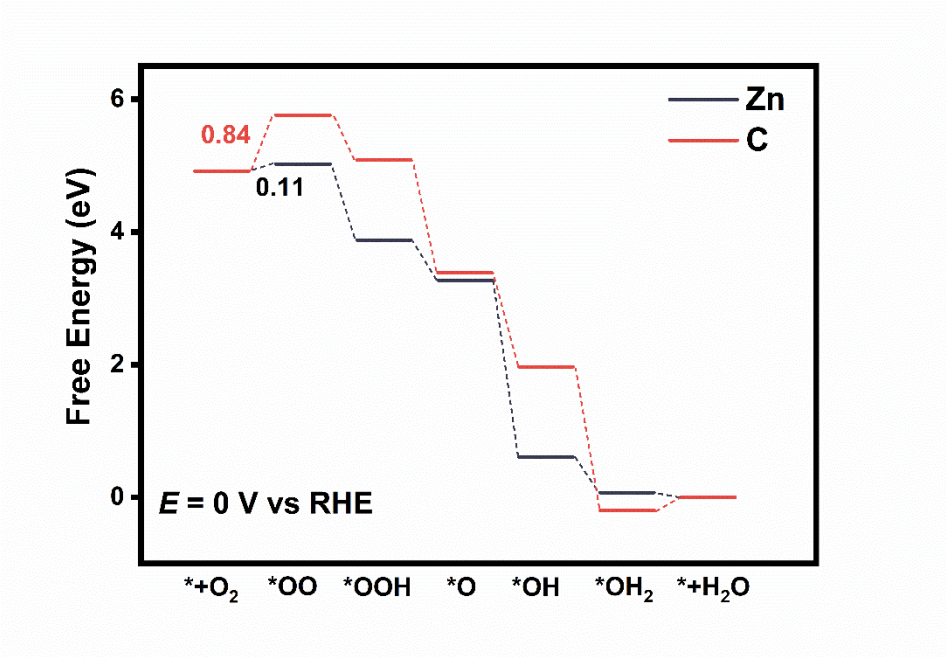

Fig. S27. The simulated energy barrier diagram at the Zn and C sites of the Zn-MCRs model at U = 0 V.

References

1 G. Kresse and J. Furthmüller. *Comput. Mater. Sci.*, 1996, **6**, 15-50.

2 G. Kresse and J. Furthmüller. *Phys. Rev. B*, 1996, **54**, 11169-11186.

3 J. P. Perdew, K. Burke and M. Ernzerhof. *Phys. Rev. Lett.*, 1996, **77**, 3865-3868.

4 G. Kresse and D. Joubert. *Phys. Rev. B*, 1999, **59**, 1758-1775.

5 M. Engel, M. Marsman, C. Franchini and G. Kresse. *Phys. Rev. B*, 2020, **101**, 184302.

6 J. K. Nørskov, J. Rossmeisl, A. Logadottir, L. Lindqvist, J. R. Kitchin, T. Bligaard and H. Jónsson. *J. Phys. Chem. B*, 2004, **108**, 17886-17892.